Neuron
NeuroResource

# Chronic Cellular Imaging of Entire Cortical Columns in Awake Mice Using Microprisms

Mark L. Andermann,[1,2,6,*] Nathan B. Gilfoy,[4,6] Glenn J. Goldey,[1,2,6] Robert N.S. Sachdev,[3,6] Markus Wölfel,[4] David A. McCormick,[3] R. Clay Reid,[2] and Michael J. Levene[4,5,*]
[1]Division of Endocrinology, Department of Medicine, Beth Israel Deaconess Medical Center, Harvard Medical School, CLS750, 330 Brookline Avenue, Boston, MA 02215, USA
[2]Department of Neurobiology, Harvard Medical School, Goldenson 243, 220 Longwood Avenue, Boston, MA 02115 USA
[3]Department of Neurobiology, Kavli Institute of Neuroscience, Yale School of Medicine, 333 Cedar Street New Haven, CT 06510, USA
[4]Department of Biomedical Engineering, Yale University, Malone Engineering Center 312, 55 Prospect Street, New Haven, CT 06511, USA
[5]Department of Neurology, Yale School of Medicine, 333 Cedar Street, New Haven, CT 06520, USA
[6]These authors contributed equally to this work
*Correspondence: manderma@bidmc.harvard.edu (M.L.A.), michael.levene@yale.edu (M.J.L.)
http://dx.doi.org/10.1016/j.neuron.2013.07.052

## SUMMARY

**Two-photon imaging of cortical neurons in vivo has provided unique insights into the structure, function, and plasticity of cortical networks, but this method does not currently allow simultaneous imaging of neurons in the superficial and deepest cortical layers. Here, we describe a simple modification that enables simultaneous, long-term imaging of all cortical layers. Using a chronically implanted glass microprism in barrel cortex, we could image the same fluorescently labeled deep-layer pyramidal neurons across their entire somatodendritic axis for several months. We could also image visually evoked and endogenous calcium activity in hundreds of cell bodies or long-range axon terminals, across all six layers in visual cortex of awake mice. Electrophysiology and calcium imaging of evoked and endogenous activity near the prism face were consistent across days and comparable with previous observations. These experiments extend the reach of in vivo two-photon imaging to chronic, simultaneous monitoring of entire cortical columns.**

## INTRODUCTION

Two-photon microscopy has become a key tool for monitoring the structure, function, and plasticity of neurons, glia, and vasculature in vivo. For all its strengths, this method suffers from two important limitations: (1) high-speed imaging is often confined to a single focal plane parallel to the cortical surface, and (2) light scattering makes it difficult to image deep cortical layers. Although deep layers of cortex such as layer 6 play a major role in regulating response amplitudes in superficial layers (Olsen et al., 2012) and in distributing information to a variety of cortical and subcortical targets (Thomson, 2010), existing methods for two-photon imaging are more effective in imaging superficial as opposed to deeper cortical layers. Further, methods currently do not exist for cellular or subcellular imaging across multiple cortical layers simultaneously.

Optical scattering degrades image quality at increasing imaging depths within brain tissue. Regenerative amplifiers (Mittmann et al., 2011; Theer et al., 2003) and long-wavelength (1,300–1,700 nm) Ti:Sapphire lasers (Horton et al., 2013) have both been used to extend the imaging depth of multiphoton microscopy, but practical limitations have restricted their use (see Discussion). Blunt-ended gradient index (GRIN) lenses have been used as implantable micro-optics for deep imaging (Barretto et al., 2011; Jung et al., 2004; Levene et al., 2004), but suffer from limited fields-of-view and significant optical aberrations, and are better suited for imaging of intact structures, such as hippocampus, rather than deep cortical layers. Traditional multiphoton imaging in certain thinner cortical areas in mice (e.g., mouse visual cortex; Glickfeld et al., 2013) can reach layers 4 and 5, but this solution often requires high average power and/or sparse labeling of neurons. Half-millimeter prisms have been used with one-photon excitation to measure the net fluorescence emission from layer 5 apical dendrites in superficial cortical layers in rats (Murayama et al., 2007), but these fluorescence images lacked cellular or subcellular resolution. Current methods allow two-photon imaging of small volumes typically spanning 50–250 μm in depth within a cortical layer, using piezoelectric scanners (Göbel et al., 2007; Kerlin et al., 2010), tunable lenses (Grewe et al., 2011), or multibeam systems (Amir et al., 2007; Cheng et al., 2011).

To rapidly obtain two-photon imaging data from a larger range of depths, we have previously shown that insertion of a sharp, 1 mm glass microprism into the neocortex of an anesthetized mouse can be used for acute, single-session two-photon imaging of anatomical structures across all six cortical layers, including the soma and dendrites of cortical layer 5 pyramidal cells, in a single field-of-view (Chia and Levene, 2009a, 2009b, 2010). Here, we describe an improved approach that has enabled chronic anatomical and functional imaging of hundreds of individual neurons and neuronal processes simultaneously

across all cortical layers. The structure and function of neurons at distances >150 μm from the prism face were not qualitatively different after prism insertion and remained stable for months after prism insertion. We also demonstrate that microprisms can be used for simultaneous, high-speed calcium imaging from neurons in layers 2 to 6 during locomotion and for imaging visual responses in long-range axon terminals in deep cortical layers. This approach complements traditional in vivo electrophysiological methods by enabling high-yield, simultaneous chronic monitoring of subcellular structure and neural activity in superficial and deep-layer cortical neurons in behaving mice.

## RESULTS

Two parallel approaches have dominated the study of neocortical circuits. One approach involves recordings in living coronal brain slices (typically ~400 μm thick). Although many long-range axonal inputs to the cortical columns within each slice are severed, this reductionist approach has provided a wealth of insights regarding the layer-specific physiological properties of neurons and the interlaminar flow of neural impulses, using multiple intracellular and extracellular recordings (e.g., Adesnik and Scanziani, 2010; Sanchez-Vives and McCormick, 2000; Thomson, 2010), two-photon calcium imaging (MacLean et al., 2006), and voltage-sensitive dye imaging (Petersen and Sakmann, 2001).

A second common approach involves neuronal recordings from the intact brain, where it is possible to correlate neural activity with sensory perception and with behavior. Two-photon imaging has provided a means for monitoring neural activity and structural plasticity across days and weeks in awake animals (e.g., Dombeck et al., 2007; Andermann et al., 2010; Mank et al., 2008; Trachtenberg et al., 2002). However, many aspects of cortical processing remain out of reach because of the challenges in imaging deep-layer neurons and in simultaneous in vivo imaging across all layers. Although such laminar recordings are possible using electrophysiological approaches (Adesnik and Scanziani, 2010; Sakata and Harris, 2009; Niell and Stryker, 2008), these methods lack fine spatial resolution and typically provide lower yield, reduced recording durations, and greater difficulty identifying cell types.

### Microprism Imaging: A Synthesis of In Vivo and Ex Vivo Approaches

Chronic two-photon imaging through a microprism combines the optical access of ex vivo brain slice preparations with in vivo behavioral context. This procedure involves insertion of a microprism attached to a cranial window (Figure 1A and Figure S1 available online). The hypotenuse of the microprism is coated with aluminum and thus serves as a right-angled mirror or "microperiscope," with a vertical field-of-view parallel to the prism face. In different experiments, we implanted a microprism into either mouse somatosensory barrel cortex or visual cortex. As described in detail below (see Experimental Procedures and Figures S1A–S1D), a microprism (barrel cortex: 1.5 × 1.5 $mm^2$ imaging face; visual cortex: 1 × 1 $mm^2$ imaging face) was glued to a coverslip. A craniotomy and durotomy were performed under sterile conditions, a small incision was made orthogonal to the cortical surface, and the microprism assembly was carefully inserted into cortex. Wide-field epifluorescence and two-photon images parallel to the cortical surface showed a vertical field-of-view across cortical layers 2–6 through the prism, revealing radial blood vessels and the expected laminar pattern of GCaMP3 expression (Figures 1B and 1C) or YFP expression (Figure 1D). The procedure for microprism insertion in the primary visual cortex (V1) (Figures 1B and 1C) involved an ~20% vertical compression of cortex (to ~675 μm in area V1) to decrease brain motion and prevent dural regrowth at the cortical surface, as in previous studies (Andermann et al., 2011; Dombeck et al., 2007).

### Chronic Translaminar Snapshots of Cortical Neurons via a Microprism Implant

We first used microprisms for chronic two-photon structural imaging of genetically labeled cortical neurons across the depth of cortex. Somata and dendrites of layer 5 neurons in barrel cortex of anesthetized Thy1-YFP-H mice were imaged immediately following and for up to 2 months after prism insertion (n = 5; Figure 1D). Large field-of-view imaging with a 4× objective immediately following prism insertion revealed labeled neurons in layers 2/3 and 5 (Figure 1D, left panel). Consistent with our earlier studies (Chia and Levene, 2009b), images included dendrites of hundreds of neurons up to depths ~900 μm below the pial surface. Imaging with a 40× objective, 29 and 68 days following prism insertion, yielded progressively clearer images, allowing visualization of fine structural details in proximal portions of layer 5 pyramidal neuron basal dendrites (Figure 1D, middle and right panels; Movie S1). The population of labeled neurons was stable over time, as demonstrated by tracking of over 40 neurons in one field-of-view across imaging sessions spaced 13 days apart (Figures S1E and S1F).

We found that when the surface of the cortex around the prism was unobstructed, the fluorescence collection efficiency was improved and "shadow" effects of radial vessels located between the image plane and the prism face were reduced. This is likely due to the diffuse nature of emitted fluorescent light, which can reach the objective through a clear cranial window surrounding the prism as well as through the prism (Figures S1G and S1H).

### Anatomical and Electrophysiological Evidence of Cortical Health after Microprism Implant

The above results indicate that neurons near the microprism face (100–300 μm away) survived prism insertion and maintained their structural integrity for months. In addition, histological evaluation with staining for hematoxylin and eosin (H&E) (Figures 1E and 1G), Nissl (Figure 1C), and DAPI (data not shown) indicated that the imaged regions were comparable to more distant brain tissue (400–500 μm away) and to neurons from nonimplanted mice (not shown). Small but significant increases in cell density were observed within the first 50 μm from the prism face ($p < 0.05$, n = 7 samples from 5 mice), followed by small but significant decreases at 50–100 μm and 100–150 μm away ($p < 0.05$) and a return to normal density beyond 150 μm from the prism (Figure 1G, all $p > 0.05$). Staining for astrocytes (anti-GFAP) and microglia (anti-CD11b), indicators of brain trauma, did not

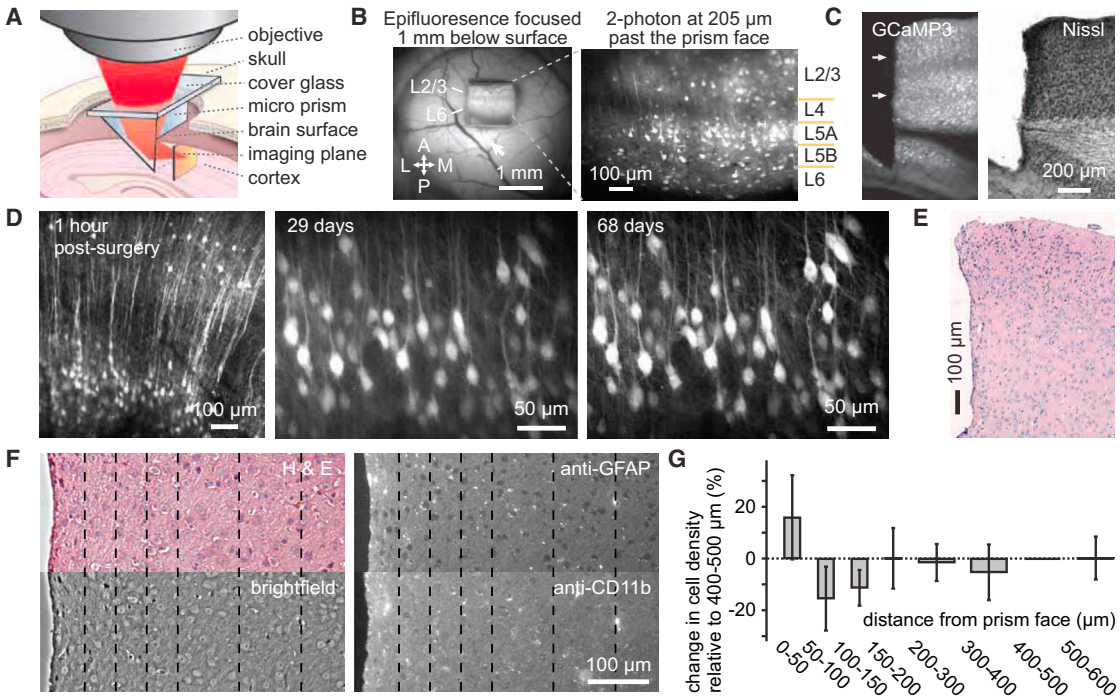


**Figure 1. Superficial and Deep Cortical Layers Imaged in a Single Plane Using a Microprism**

(A) Illustration of beam path through a prism implanted into neocortex. The reflective hypotenuse of the prism converts the horizontal imaging plane into a vertical plane.

(B) Left: widefield epifluorescence image of a 1 mm prism implanted in visual cortex, focused 1 mm below the cortical surface. Fluorescent expression of AAV-GCaMP3 can be seen through the cranial window (arrow) and through the prism. Right: two-photon image taken through the same prism (maximum intensity projection across 15 min of recording) at 205 μm lateral to the microprism imaging face, 21 days after prism implant.

(C) Laminar locations were obtained from postmortem histological sections of GCaMP3 expression (left) and Nissl stain (right) after removal of the prism (black triangular hole; original imaging path indicated by arrows).

(D) Anatomical images of cortex taken though a prism at different times after surgery in a Thy1-YFP mouse. Within the first hour after prism insertion, cell bodies in layers 2/3 and 5, and neuronal processes throughout the cortical depth, are visible in a single frame taken 200 microns lateral from the prism face (left panel). An increase in imaging quality over time can be seen on the same population of layer 5 neurons at 29 and 68 days after surgery (middle and right panel, respectively. Images are maximum projections over 76 frames taken from 40 μm to 270 μm lateral to the prism face.).

(E) Histological section of H&E staining after removal of prism.

(F) Tissue morphology appears normal at distances of more than 150 μm from the prism face. H&E staining and brightfield illumination show that cell density is slightly changed proximal to the prism face (left border). Staining for astrocytes (GFAP) and microglia (CD11b) appears normal at 27 days after implant.

(G) With increasing distance from the prism face, cell density first increases, then decreases and reaches normal amounts within the first 150 μm. For each of seven samples, cell counts were normalized to those from 400–500 μm from the prism. Error bars represent SE.

See also Figure S1 and Movie S1.

show evidence of chronic tissue scarring at 27 days after surgery (Figure 1F). These data are consistent with studies showing a persistent macrophage response <50 μm from chronically implanted electrodes with decreased neuronal density at 0–150 μm from the electrode (Biran et al., 2005). These data are also consistent with our previous studies using acute microprism implants, in which propidium iodide staining demonstrated that neuronal damage was limited to <150 μm from the prism face (Chia and Levene, 2009b). Nevertheless, a key question is whether the prism implant causes spreading depression, silencing, or other major changes in activity of local cortical neurons at distances >150 μm from the microprism face.

We confirmed the sustained presence of generally normal spontaneous activity at distances of ~100–200 μm from a chronically implanted prism using multi-unit recordings of endogenous and stimulus-evoked activity in cortical layer 5 using repeated penetrations with tungsten microelectrodes in ketamine/xylazine anesthetized mice (see Figure S2A; Supplemental Experimental Procedures; n = 3 animals). Neurons showed similar characteristic fluctuations between Up and Down states of spontaneous activity (e.g., Ros et al., 2009), before prism implantation, as little as 10 min after prism implantation, as well as 3 days and 120 days after implantation (Figures S2B–S2E).

Multiunit responses to air-puff stimulation of facial vibrissae revealed that tactile sensory inputs to neurons near the prism face also remained largely intact, demonstrating localized and spatially specific responses with similar response latency (~15–20 ms following air-puff onset) and dynamics between recordings prior to and immediately following implantation (Figures S2F and S2G).

Together, these data suggest that the thalamic and cortico-cortical input that generates the short and long latency

components of the sensory-evoked responses were generally intact in neurons >100–150 μm from the prism face. These results provided the impetus for determining whether two-photon imaging of calcium activity in neurons via a microprism could be achieved in the visual cortex of awake behaving mice.

### Chronic Microprism Imaging of Visual Response Properties in Behaving Mice

We obtained stable, chronic recordings of calcium activity across cortical layers as follows: first, a headpost was affixed to the skull and a 5 mm craniotomy was performed over mouse visual cortex. A standard cranial window was then installed (8 mm round coverslip glued above two 5 mm round coverslips to slightly compress the brain, reducing brain motion and regrowth; see Figures S1A–S1D; Andermann et al., 2011). Cortical expression of the genetically-encoded calcium indicator, GCaMP3 (Tian et al., 2009), was achieved using adeno-associated virus (AAV) injection in layers 2/3, 5, and 6. Following recovery from surgery, mice were trained to tolerate several hours of head restraint (see Experimental Procedures and Andermann et al., 2011).

Subsequently, the original cranial window (Figures S1A and S1B) was removed under anesthesia and replaced by a microprism assembly (Figures S1C and S1D; Experimental Procedures) consisting of a microprism glued to three layers of coverglass. Gluing the microprism in a specific, predetermined location relative to the cranial window allowed (1) targeted insertion in posterior V1 near the site of GCaMP3 expression, (2) minimization of damage to large surface vasculature, and (3) orientation toward posterior and lateral cortex (Figure 1B) to minimize damage to thalamocortical axons from the lateral geniculate nucleus (which traverse cortex from lateral to medial, below layer 6, before ascending into their target cortical column; Antonini et al., 1999).

Before imaging GCaMP3 activity through a microprism, we evaluated how the implant of a prism influences the sensory response properties of nearby neurons. We first measured the visual response properties of neurons through a standard cranial window and then assessed the response properties of the same neurons following insertion of a microprism at a distance of 350 μm away (Figure 2A, white dashed squares, and 2B). We used an identical approach across sessions—two-photon volume imaging of visual responses of GCaMP3-expressing layer 2/3 neurons through the cranial window in an awake, head-fixed mouse that was free to run on a linear trackball (Experimental Procedures; Glickfeld et al., 2013). The insertion of the microprism resulted in the accumulation of some blood at the brain surface and prism surface, which cleared up over the course of several days (Figures 2A and S2H–S2M). Major surface vessels >150 μm from the prism face remained intact, and no obvious changes in blood flow through these vessels were observed during or after prism insertion. In the volume of imaged neurons (330 μm × 350 μm, 70–163 μm below the cortical surface), surface vascular patterns and baseline GCaMP3 expression in neurons were also similar prior to and in the days following prism insertion (Figure 2B; see also Figures S2H–S2L). Perfusion was maintained over days at the prism surface by persistence of some local vasculature as well as neovascularization (Figure S2M).

We evaluated visual response properties of neurons near the prism by presenting drifting gratings in one of 16 directions and one of two spatial frequencies (0.04 and 0.16 cycles/deg; Andermann et al., 2011). Volume imaging (31 planes spaced 3 μm apart, imaged at 1 Hz with a 32 Hz resonance scanning microscope; Bonin et al., 2011; Glickfeld et al., 2013) allowed accurate correction for small changes in imaging depth within and across sessions. During the session prior to prism implant, we found 44 neurons with significant visual responses (Bonferroni-corrected t tests) and measurable preferences for stimulus direction (bootstrapped confidence interval <60°, see Andermann et al., 2011). Reimaging at 1 day following prism implant yielded 27 neurons that met the same criteria, of which 23 were confirmed (by inspection of baseline GCaMP3 volume stacks) to match neurons that were driven preimplant (see below). Example polar plots of normalized direction tuning from three of these neurons (Figure 2C) show consistent tuning properties that also persisted in subsequent imaging sessions (4 and 5 days postimplant). Direction preferences were remarkably similar for all neurons characterized 2 days prior to and 1 day after prism implant (Figure 2D, top panel). The small residual mean absolute difference in preference (8.1° ± 1.6°) was smaller than our sampling resolution (22.5°) and persisted in later imaging sessions (Figure 2F).

Our index of direction selectivity, defined as the relative response strength for preferred versus antipreferred directions, showed a marginal increase following prism implant (Figure 2E, middle; paired t test, $p = 0.048$ 1 day postimplant, $p > 0.05$ at 4 and 5 days postimplant; see also Figure 2G; Experimental Procedures). Peak responses decreased by 30%–35% following prism implant (Figure 2E, bottom; paired t test, $p = 0.038$, 0.036, 0.007 at 1, 4, and 5 days postimplant; Figure 2H). Although this decrease in response strength could, in principle, influence direction selectivity (given the sublinear properties of GCaMP3 at low spike rates; Tian et al., 2009), we found no correlation between changes in peak response strength and changes in direction selectivity in any postimplant imaging session (all p values > 0.05). However, this decrease in response strength, coupled with the rectifying properties of GCaMP3, may contribute to the concomitant decrease in number of significantly driven neurons observed following prism implant (Figure 2I). Specifically, we found that of the neurons with significant responses and measurable direction tuning preimplant, 75% (33/44) were also responsive in at least one of the three imaging sessions postimplant. Our inability to recharacterize the remaining 25% of these neurons postimplant may be due to the reduction in response strength, as well as session-to-session changes unrelated to prism implant, including variations in arousal and eye position. Critically, none of the observed changes in direction preference, direction selectivity or peak response amplitude were correlated with distance from the prism face during any of the three postimplant sessions (Figure 2E, Pearson's correlation, all p values > 0.05). These results are consistent with our anatomical results (Figure 1) indicating uniform cell health at distances >150 μm from the prism face.

To test whether we could observe visual responses through the microprism, we performed simultaneous visual mapping of individual neurons across all cortical layers of awake mouse

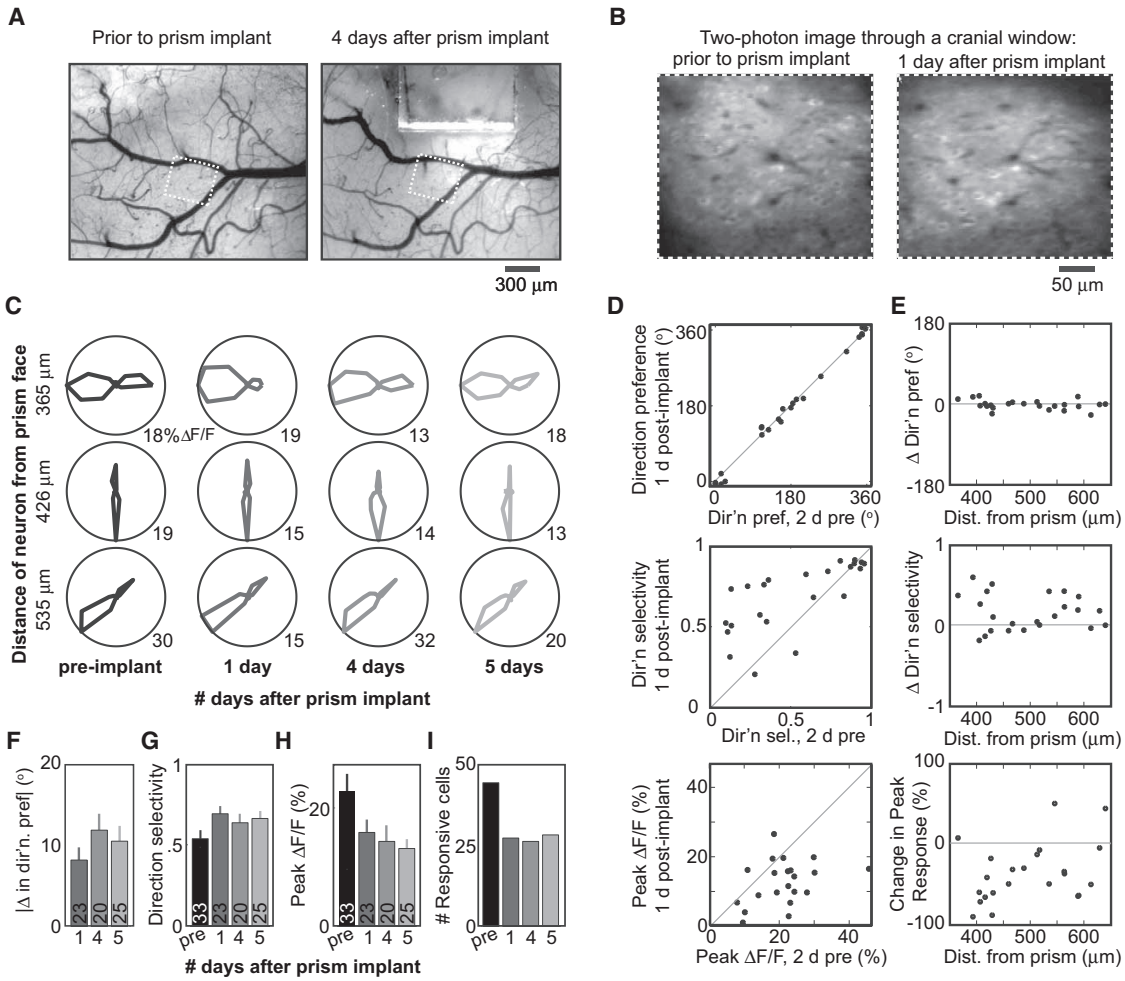


**Figure 2. Comparison of Cortical Neuron Responses prior to and after Prism Implant**

(A) Brightfield image through a cranial window, prior to and 4 days after prism implant (see also Figure S2).

(B) Two-photon imaging of GCaMP3 expression in awake mouse primary visual cortex (V1) in the same field of view (dashed box in A), 2 days prior to and 1 day after prism implant (depth: 103 μm).

(C) Polar plots of normalized visual responses to 16 directions of motion in three example neurons at varying distances from the prism face, across four sessions (2 days prior, and 1, 4, and 5 days after prism implant). Peak response amplitudes (% ΔF/F) noted at bottom right.

(D) Comparison of direction preference (top panel), direction selectivity (middle panel), and peak response amplitude (lower panel) for all responsive neurons with reliable direction preference, 2 days prior and 1 day after implant.

(E) None of the differences in response properties prior to versus after prism implant varied with the neurons' distance from the prism face.

(F–I) The absolute change in direction preference from 2 days prior to 1, 4, or 5 days after implant was smaller than the sampling resolution of 22.5° (F). Average direction selectivity (G) increased across sessions, whereas peak amplitude (H) and number of responsive neurons (with measurable direction preference) (I) decreased after prism implant. Sample numbers in (F)–(H) (indicated on each bar) include all neurons significantly driven both prior to and on a given day after prism implant, whereas numbers in (I) include all responsive neurons (with measurable direction preference) during any given session. Error bars represent SE.

V1. We presented oriented, square-wave drifting grating stimuli (Experimental Procedures; Andermann et al., 2011) in two retinotopic locations, 12 directions, two spatial frequencies (0.04 and 0.16 cycles/degree), and two temporal frequencies (1 and 4 Hz). Two-photon calcium images, acquired at 1 Hz, spanned 600 μm × 900 μm—sufficient to encompass cortical layers 2 to 6.

In a typical session (Figure 3A; 205 μm past the prism face, 21 days following prism insertion, 45 mW power at the sample), we observed visually evoked responses in over one hundred neurons across all cortical layers (see also Movie S2). To visualize the density of responsive neurons, we plotted a maximum intensity projection of increases in GCaMP3 calcium indicator fluorescence across average response maps for each of the 96 stimulus conditions (Figure 3A; see Experimental Procedures). We estimated the laminar identity of each neuron by comparing ex vivo images of GCaMP3, DAPI and Nissl staining with in vivo baseline GCaMP3 images, which displayed a characteristic laminar expression pattern that peaked in layer 2/3 and in upper layer 5 (Figures 1B and 1C; data not shown).

We first analyzed the neurons' orientation preference. Neurons in all cortical layers demonstrated orientation tuning curves

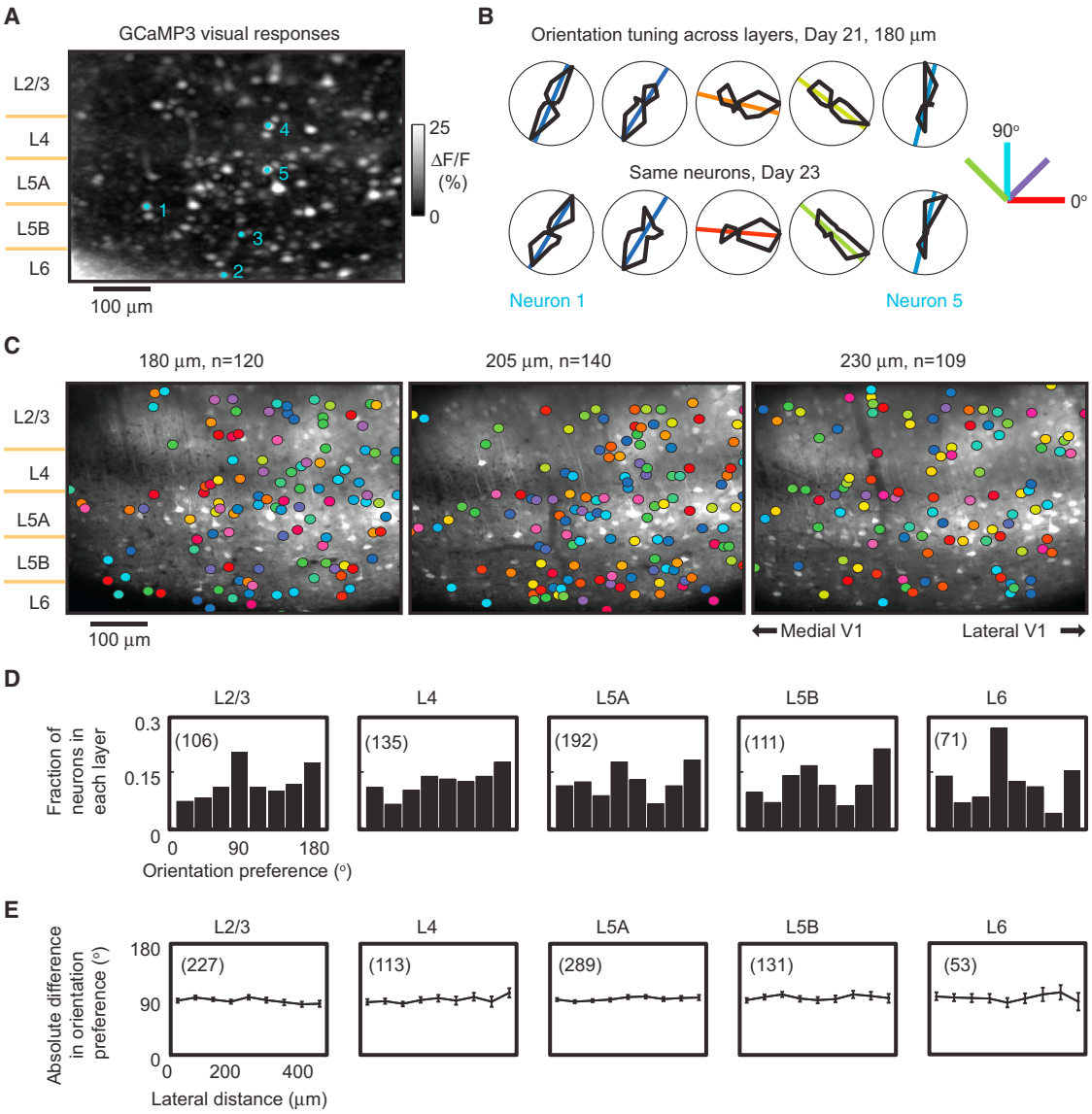


**Figure 3. Long-Term Imaging of Orientation Preference across All Cortical Layers in Awake Mouse V1**

Neural activity was imaged through a microprism at 1 Hz across all cortical layers during presentation of visual stimuli.

(A) Maximum intensity projection of fractional change in GCaMP3 fluorescence (ΔF/F), computed across a stack of average visual response maps for each of 96 stimulus conditions. Data were collected 23 days after prism implant, 180 μm from the prism face. Visually responsive neurons (white spots) were evident in all cortical layers. Bright signal (ΔF/F) at lower left is due to very low baseline fluorescence (F) in that region of the image.

(B) Neurons across all cortical layers (numbered in blue in A) showed sharp orientation tuning that was consistent at days 21 and 23 following prism implant. Orientation tuning curves are averaged across stimulus locations, spatial and temporal frequencies, and normalized by peak response. Colored lines and colored inset in polar plots indicate estimates of orientation preference (see Experimental Procedures). These five neurons had strong responses in both sessions, exceeding 30% ΔF/F for the preferred orientation.

(C) Such estimates were used to generate orientation preference maps across cortical layers, across imaging sessions (on days 21, 24, and 27 following prism implant) at three distances from the prism face (180 μm, 205 μm, 230 μm, respectively).

(D) Layer-specific population analyses (numbers in parentheses) from these data, together with three additional sessions from another mouse, revealed distributions of orientation preference with typical biases toward cardinal orientations (Roth et al., 2012).

(E) The mean absolute difference in orientation preference did not depend on the horizontal distance between neurons, extending previous imaging findings of a lack of clustering for orientation preference in rodent V1 (e.g., Ohki et al., 2005, Kerlin et al., 2010) to deeper cortical layers. For each layer, n indicates the median number of cell pairs in a given bin (bin size: 50 μm).

See also Movie S2.

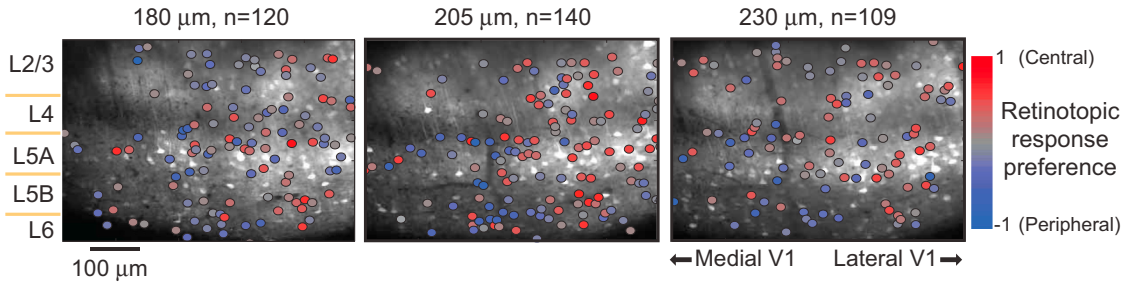


**Figure 4. A Coarse Retinotopic Map Exists in All Cortical Layers of Awake Mouse V1**

Retinotopic preference for the location of the Gabor-like drifting grating stimuli (positioned at a more central location (~45°) or a more peripheral location (~65°)), plotted for the same imaging sessions and neurons described in Figure 3C. Preference index: $(R_{central} - R_{peripheral})/(R_{central} + R_{peripheral})$. These data extend previous findings of fine-scale scatter but coarse retinotopic progression (Bonin et al., 2011; Smith and Häusser, 2010) to deeper layers of mouse V1. See also Movie S2.

generally similar to previous electrophysiological reports (Figure 3B, left column; Niell and Stryker, 2008). Orientation tuning curves imaged through the prism were stable across multiple days (Figure 3B), consistent with previous studies in layer 2/3 of mouse V1 (Andermann et al., 2010; Mank et al., 2008).

Figure 3C illustrates the orientation preference of neurons throughout the depth of mouse V1 for all responsive neurons (see Experimental Procedures) for which a reliable estimate of orientation preference was possible (bootstrapped confidence interval <60°; Andermann et al., 2011). The three imaging planes in Figure 3C were recorded 21, 24, and 27 days after prism implant, at distances of 180 μm, 205 μm, and 230 μm beyond the prism face, respectively. We analyzed orientation preference from these sessions and from three sessions in a second prism-implanted mouse. Consistent with previous reports in superficial cortical layers, we did not find any evidence of columnar clustering of orientation preference in any cortical layer (Figures 3C and 3D). Distributions of orientation preference showed typical biases to cardinal orientations across all layers, also consistent with previous reports (Figure 3E; Andermann et al., 2011; Roth et al., 2012).

The same data sets presented in Figure 3B could also be used to estimate relative retinotopic preference of mouse V1 neurons for one of two horizontal stimulus locations, spaced 20° apart (Figure 4). Consistent with previous reports in superficial layers, neurons showed a coarse progression of retinotopic response preferences in all cortical layers, as well as some degree of local scatter (Bonin et al., 2011; Smith and Häusser, 2010). Taken together, these data demonstrate broadly normal orientation and retinotopic response properties in neurons at several hundred microns from the prism face, providing further evidence that microprism implants provide a viable means for simultaneous monitoring of neuronal activity in all layers of neocortex across weeks.

## Microprism Imaging of Long-Range Axonal Boutons

A unique advantage of two-photon imaging is the ability to monitor subcellular structures, such as dendrites (Figure 1) and axons. Recently, we and others have described functional imaging of long-range projection axons using GCaMP3 in awake mice (Glickfeld et al., 2013; Petreanu et al., 2012). Because of the small size of individual axons and synaptic boutons, functional imaging of axons has been restricted to superficial depths in cortex (~0–150 μm deep). However, many classes of projection neurons selectively innervate deep cortical layers (e.g., Petreanu et al., 2009). To determine whether use of a microprism could enable monitoring of long-range axonal activity deep within the cortex, we made a small injection of GCaMP3 into area V1 (Glickfeld et al., 2013) and inserted the prism into the posteromedial secondary visual cortical area (PM), an area densely innervated by V1 axons, with the prism oriented to face area V1. We could visualize characteristic patterns of axons and putative boutons in a 75 μm × 75 μm field of view, located 100 μm in front of the prism face and 200–275 μm below the cortical surface (Figure 5A), at 10 days following prism implant. Endogenous coactivation of multiple boutons along each of two axonal arbors is shown in Figures 5B and 5C. We also observed robust visual responses of individual boutons at depths of 480–510 μm below the cortical surface (putative layer 5) during presentation of stimuli at multiple temporal frequencies (1–15 Hz) (Glickfeld et al., 2013) and spatial frequencies (0.02–0.16 cyc/deg) at 1 day postimplant (see Figures 5D–5F; Experimental Procedures; Movie S3). Recording quality was sufficient to obtain spatiotemporal frequency response tuning estimates for individual boutons (Figure 5E; cf. colored arrows in Figure 5D and single-trial responses in Figure 5F).

## High-Speed Cellular Imaging of Endogenous Activity across All Cortical Depths

Simultaneous imaging of all cortical layers allowed direct examination of interlaminar neural dynamics, on a trial-by-trial basis, in awake mice that stood or ran on a linear trackball, as shown in Figures 6A and 6B and Movie S4. Using a fast, resonance-scanning two-photon microscope (~32 Hz frame rate, 720 μm × 720 μm, 256 × 240 pixels/frame; see Experimental Procedures and Bonin et al., 2011), we were able to measure endogenous neural activity simultaneously in 208 neurons spanning all six cortical layers of V1. Data were collected in near-complete darkness from the same mouse as in Figure 3, 38 days after prism implant, ~140 μm from the prism face.

This data set provided a proof of principle demonstration of the capacity of chronic microprism imaging for examining changes in neural activity across layers following the onset of running bouts (Figures 6E and 6F; Movie S5; average of all 53 running onsets from the 20 min recording session, each

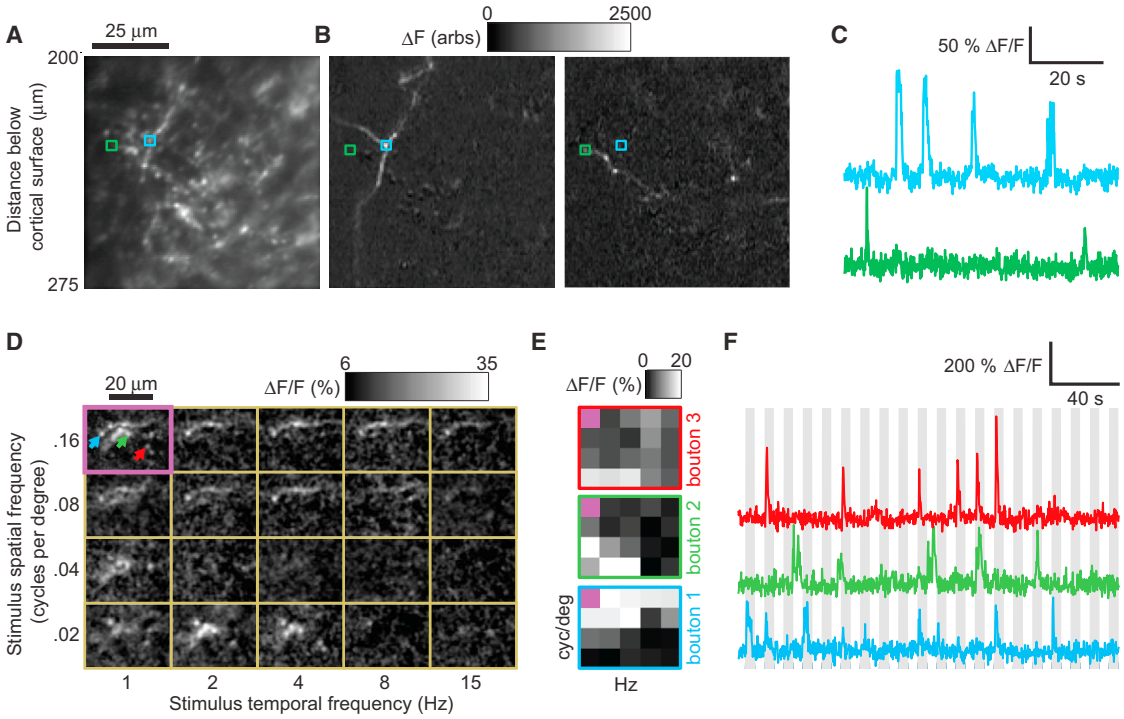


**Figure 5. Microprism Imaging of Neural Activity in Long-Range Axons of V1 Projection Neurons**

To image long-range cortico-cortical axonal arbors in awake mice through a prism (Glickfeld et al., 2013), AAV-GCaMP3 was injected into area V1 and a microprism was subsequently inserted at the site of V1 innervation of posteromedial secondary visual area PM.

(A) Two-photon imaging (100 μm from the prism face, 200–275 μm deep, 10 days after prism implant) of baseline GCaMP3 fluorescence in long-range V1 axons (thin white lines) and putative V1 axonal boutons (small white spots) in area PM.

(B) Fluorescence activation (white) of two axonal arbors in this field of view during two representative endogenous events (average of 2 s of data). ΔF: change in fluorescence, in arbitrary units.

(C) Fluorescence time courses (4 Hz) of endogenous activity from segments of the two axons (blue and green squares in A and B).

(D–F) Robust visually evoked activity was observed in V1 axonal boutons innervating deeper layers of area PM (480–510 μm below the cortical surface) in the same mouse (1 day postimplant). (D) Response maps to upward drifting stimuli varying in spatial and temporal frequency, as in Glickfeld et al. (2013). Distinct boutons (white spots) were activated by different visual stimuli. Purple square at top left: Maximum intensity projection of all response maps; colored arrows point to three active boutons. (E) Spatial-temporal frequency receptive fields (evoked response to each stimulus condition in D for each of these three boutons). (F) Associated time courses demonstrated robust single-trial responses to visual stimulation (gray bars), no fluorescence crosstalk, and little photobleaching (data not shown).

See also Movie S3.

preceded by >2 s of immobility and followed by sustained locomotion >2 s; see Experimental Procedures). We observed neurons whose average endogenous activity increased at running onset and other neurons whose activity consistently decreased at running onset (black dots in Figure 6F, paired t test, $p < .05/208$; see also Figures 6C–6E and 6G). Intriguingly, the strongest suppression of endogenous activity was observed in several layer 6 neurons (Figures 6D–6F; Movie S5).

To better understand these changes in neuronal activity across layers, we also examined changes in activity across individual running onsets (Figure 6G). Although such activity changes typically had the same sign for each neuron, different neurons demonstrated different degrees of trial-to-trial variability (compare reliability of neurons at depths of 288, 554, and 581 μm in Figure 6G). In particular, most pairs of neurons had relatively low trial-to-trial covariability (Figures 6G and 6H). For example, of the 21,528 pairs of simultaneously recorded neurons in this data set, only 11% had a correlation of magnitude >0.2. These data illustrate the rich repertoire of inter- and intralaminar neural dynamics accessible using microprism-based columnar recordings in behaving animals.

## DISCUSSION

We have developed a broadly applicable method for chronic, large-scale, and simultaneous in vivo two-photon anatomical and functional imaging across all cortical layers of awake mice. Our use of a reflective glass microprism minimizes the distance that excitation photons must travel through scattering tissue to reach deep cortical tissue (Figure 1A). Thus, this method maintains high spatial resolution across layers while requiring only moderate laser power.

As discussed below, our combination of electrophysiological recordings, anatomical, and functional imaging, as well as post hoc histological analyses, attest to the viability of imaged neural cell bodies, dendrites, and axons several hundred microns from

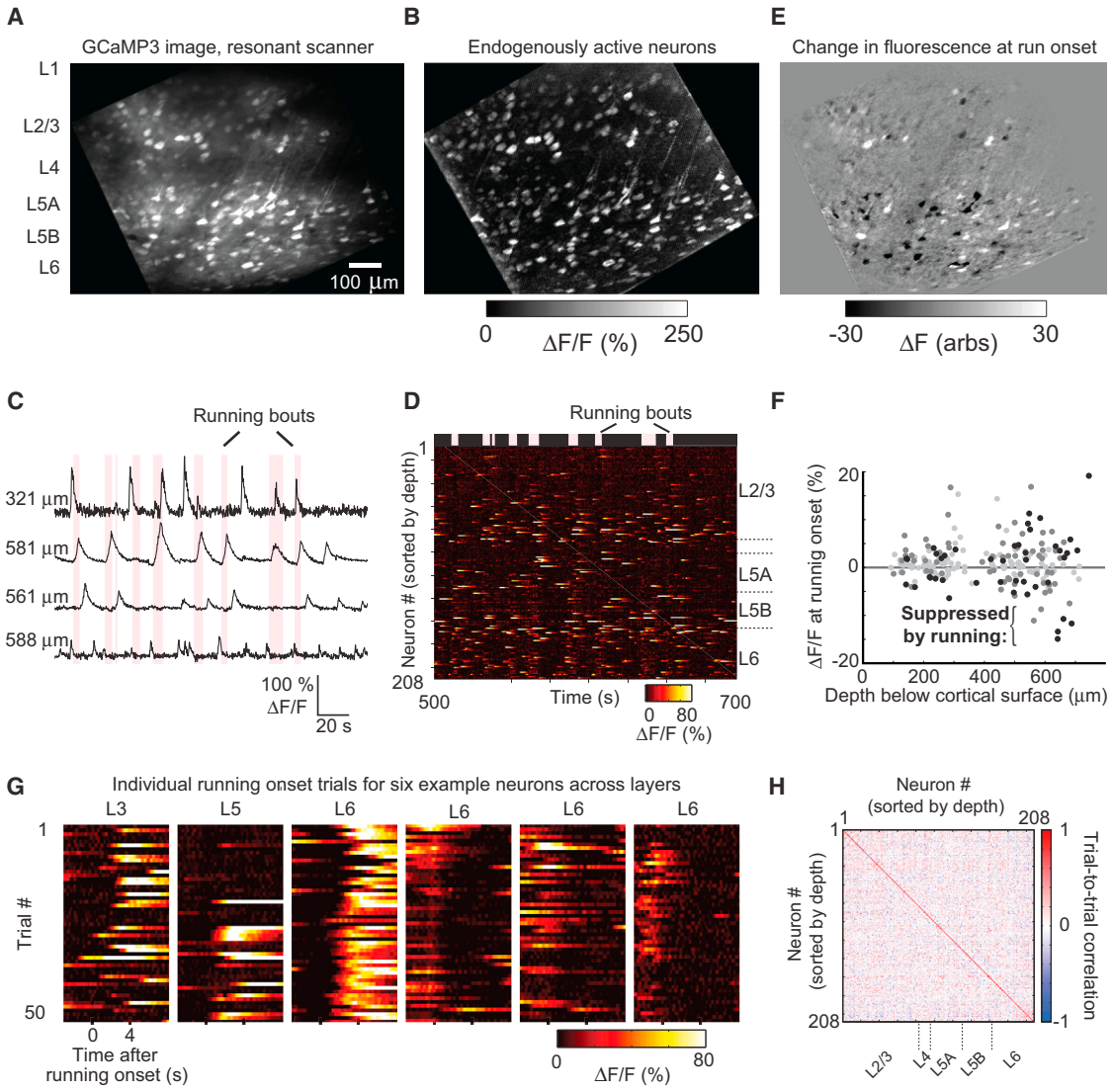


**Figure 6. Simultaneous Cellular Imaging of Running-Related Changes in Activity across All Cortical Layers**

Rapid endogenous dynamics of cortical activity was imaged at 32 Hz across entire cortical columns in awake mice that were free to run on a linear trackball in near-complete darkness. The series of images recorded in a 20 min session was downsampled to 16 Hz and coregistered (see Experimental Procedures).

(A) Maximum intensity of GCaMP3 fluorescence across the entire recording at ~140 µm from the prism face. The image has been rotated by 150° so that layer 2/3 is at the top and layer 6 is at the bottom.

(B) Over 200 neurons in the field-of-view were endogenously active and were monitored simultaneously across layers, as shown in a maximum intensity projection across the entire recording after normalization to median fluorescence, $(F(t) - F_{median})/F_{median}$.

(C) Time courses of four of the simultaneously recorded neurons (one in layer 2/3 and three in deep layers; corrected for neuropil contamination). Pink shading indicates bouts of locomotion. Some neurons were active during locomotion, whereas others were more active during rest.

(D) Time courses for all 208 simultaneously recorded neurons, plotted together with bouts of running (pink blocks at top).

(E) Change in GCaMP3 fluorescence, between the 2 s prior to and 2–3 s after locomotion onset. Black regions indicate neurons whose endogenous activity is suppressed by running, white regions indicate neurons activated by locomotion.

(F) Diverse changes in neural activity at running onset were observed across cortical layers, including many deep-layer neurons exhibiting strong running-induced suppression. Fractional change in GCaMP3 fluorescence at running onset, $(F_{run} - F_{still})/F_{still}$, where $F_{still}$ is the average fluorescence in the 2 s prior to locomotion onset and $F_{run}$ is the fluorescence from 4–6 s after locomotion onset. Black dots: paired t test, $p < 0.05$; dark gray dots: $p < 0.05/208$, light gray dots: all other neurons.

(G) For six of these neurons, endogenous activity is plotted for all 53 individual locomotion onset trials (depth from left to right: 288 µm, 554 µm, 581 µm, 642 µm, 643 µm, 688 µm). Note that a neuron's activity could be highly variable across trials.

(H) Despite this high trial-to-trial variability, pairs of neurons within and across layers did not show consistently strong covariation in activity across trials (Pearson's correlation).

See also Movies S4 and S5.

the prism face, across all cortical layers. Long-term imaging of the same neural cell bodies, dendrites, and axons across cortical layers should enable a wide range of morphological and functional experiments geared toward understanding inter- and intralaminar cortical plasticity and dynamics in healthy animals and in models of disease progression.

## Basic Properties of Local Cortical Circuits Appear Intact across Months after Implantation

We demonstrated chronic two-photon imaging of neurons for months after prism implantation. Although images can be obtained on the day of surgery (Chia and Levene, 2009b), they were sometimes less clear and required somewhat higher laser power. In these cases, imaging clarity improves over subsequent days. This initial clouding could be due in part to gliosis (Barretto et al., 2011). However, the time course of immediate clouding and subsequent improvement in clarity is more consistent with clearing of blood at the prism and cortical surfaces (Figures S2H–S2M; see also Chia and Levene, 2009b).

The chronic implantation of a 1 mm prism involves severing of some horizontal cortical connections. Thus, as with live imaging studies using coronal brain sections, it is important to carefully assess whether the local cortical circuitry near the prism imaging face is sufficiently preserved to provide meaningful anatomical and functional data. We therefore undertook a multitiered approach, using functional and anatomical imaging, microelectrode recordings, and histological staining, to show that the basic cell health and receptive field properties of neurons at >100–150 μm lateral to the prism face are qualitatively similar to what is observed in experiments not involving chronically implanted prisms.

Multiunit electrophysiological recordings from barrel cortex demonstrated that cortical neurons close to the prism face were endogenously active and responsive to whisker stimulation at 10 min, 3 days, and 120 days postimplant. Even immediately following prism insertion, ketamine-induced oscillations in spiking persisted, with normal tactile response latencies and intensities. We did note a temporary increase in sustained spiking activity immediately following prism insertion (suggesting damage to a subset of neurons), but we did not observe spreading depression or acute silencing of cortical activity.

Epifluorescence and two-photon imaging demonstrated blood perfusion in intact radial vessels at distances of >50 μm from the prism face (Figures 2A, 2B, and S2H–S2M; Chia and Levene, 2009b). Functional and anatomical imaging of the same neurons across weeks (Figures 2, 3, and S1) and across sessions both prior to and following prism insertion, suggests that most neurons at >150 μm from the prism face did not undergo damage-induced cell degeneration or death. Consistent with previous studies (Niell and Stryker, 2008, 2010; Olsen et al., 2012), we observed sharp orientation tuning in neurons in all cortical layers of mouse V1 (Figure 3B), at distances of ~200 μm from the prism face. Critically, orientation and direction tuning in the same neurons was largely stable across days, both prior to and following prism implant. Further, these data confirmed that superficial layer neurons in mouse V1 are not spatially clustered by preferred stimulus orientation (Dräger, 1975) but do exhibit a coarse retinotopic map (e.g., Bonin et al., 2011; Smith and Häusser, 2010) and extended these findings to deeper layers (see also Dräger, 1975).

We did observe an average reduction in peak response strength of 30%–35% in the days immediately following prism insertion, and we were only able to characterize visual responses in 75% of neurons that were visually responsive in the preimplant imaging session. Although the decreases in response strength and in the number of responsive neurons may indicate an influence of the prism implant on neural excitability, changes in response strength did not depend on a neuron's distance from the prism face (Figure 2E), thus indicating possible contributions from additional factors such as residual postsurgical inflammation or intersession variability in arousal or eye position.

In addition to long-term imaging of neurons and dendrites across cortical depths, we could also image the activity of long-range projection axons of V1 neurons in secondary visual area PM in awake mice. Putative axonal boutons demonstrated both endogenous and stimulus-evoked activity (Figure 5). Thus, this method extends the recently described technique of in vivo functional imaging of axonal arbors (Glickfeld et al., 2013; Petreanu et al., 2012) to imaging of arbors of identified classes of local or interareal projection neurons that specifically innervate deeper cortical layers (e.g., Petreanu et al., 2009). Further, the study of long-range projection axons via a microprism represents a less invasive application of this method with fewer caveats than for imaging of cell bodies near the prism face: while damage to long-range axonal boutons near the prism face cannot be ruled out, these boutons report the activity of neurons whose dendrites are safely located millimeters from the prism implant.

## Interlaminar Patterns of Endogenous Cortical Activity in Behaving Mice

These experiments demonstrate that two-photon imaging via a microprism can provide unique insights into local functional organization in the deepest cortical layers. A key additional feature of our approach is the ability to investigate interlaminar cortical dynamics of evoked and endogenous activity on single trials (Figure 6) across timescales from milliseconds and seconds to days and weeks, providing a powerful complementary approach to electrophysiological methods (Sakata and Harris, 2009; O'Connor et al., 2010). A previous report described increased neural activity in layer 2/3 of V1 during locomotion in darkness (Keller et al., 2012). In our example data set, we observed a diversity of dynamics across neurons and cortical layers, consisting either of increases, decreases, or no change in activity at onset of locomotion. The strong decrease in endogenous activity we observed in a handful of layer 6 neurons during locomotion has not been previously reported, but is consistent with recent evidence suggesting that decreases in layer 6 activity may increase gain in other cortical layers via release of inhibition (Olsen et al., 2012). Future studies could use chronic microprism imaging to investigate how changes in deep-layer neurons may influence running-related increases in visual response gain in superficial cortical layers (Niell and Stryker, 2010). Similarly, future analyses of trial-to-trial covariability in activity of neurons across cortical layers (Figures 6G–6H) may help identify interlaminar assemblies within a cortical column.

## Comparison to Other Deep Imaging Methods

The microprism approach presented here is relatively simple, inexpensive (~$50 per prism), and fully compatible with standard, commercially available multiphoton microscopes. In addition, because it does not require unconventional laser sources or wavelengths, microprism imaging is flexible enough to be used in combination with a wide range of fluorescent dyes. Visualizing all six layers of cortex in a single field-of-view makes microprisms compatible with high-frame rate imaging methods that employ resonant scanners, multiple beams, or acousto-optic deflectors. Critically, our method addresses two major obstacles to expanding the use of in vivo two-photon microscopy: cellular imaging in deeper cortical layers with high sensitivity and contrast, and imaging of multiple cortical layers in a single field-of-view. As discussed below, several other methods have been developed to address each of these limitations individually.

Depth penetration using two-photon imaging is primarily limited by scattering of the excitation light, whereas fluorescence collection efficiency is much less sensitive to imaging depth (Centonze and White, 1998; Denk et al., 1994; Dunn et al., 2000; Zinter and Levene, 2011). Successful approaches for imaging at greater depths within cortex have therefore concentrated on increasing the penetration of near-infrared laser light. Regenerative amplifiers decrease the duty cycle of the laser pulses by a factor of ~400, resulting in up to ~400-fold increases in two-photon-excited fluorescence for the same average power. Regenerative amplifiers have been used to compensate for loss of ballistic excitation photons while imaging as deep as 800 μm below the cortical surface (Mittmann et al., 2011; Theer et al., 2003). However, the much slower repetition rate (200 kHz), greater risk of two-photon photo damage, and lack of wavelength tunability of these systems complicates their use.

Use of 1,280 nm or 1,700 nm excitation light takes advantage of decreased light scattering at longer wavelengths and has been used to image dye-loaded vasculature and red-fluorescent-protein-labeled neurons down to 1.6 mm below the cortical surface (Horton et al., 2013). However, this technique is not currently suitable for functional imaging, as most calcium-sensitive dyes require excitation at shorter wavelengths. Blunt-ended gradient index (GRIN) lenses have been used as implantable micro-optics for deep imaging (Barretto et al., 2011; Jung et al., 2004; Levene et al., 2004), however, they suffer from limited fields-of-view and significant optical aberrations. Importantly, the limited working distances of these lenses precludes use in deep-layer cortical imaging without lens insertion directly into the overlying neuropil, resulting in severe damage to the imaged cortical column. In limited situations, such as imaging in mouse V1, the cortex is only ~850 μm thick (Paxinos and Franklin, 2001; prior to a ~20% compression by the cranial window), making it possible to image GCaMP3 activity in cell bodies down to layer 5 (~550 μm deep) using a standard chronic cranial window and a very high NA objective (Glickfeld et al., 2013). However, even in such instances, the deepest layers of cortex cannot be accessed, nor can multiple layers be imaged simultaneously. For imaging in other cortical regions of mouse (e.g., mouse SI, 1,250 μm thick) or in most other mammalian cortices (e.g., rat V1, 1,350 μm thick; macaque V1, ~3,000 μm thick), the use of a microprism may be critical for achieving high-resolution functional imaging in cortical layers 4, 5, and 6.

Other techniques have also attempted to image multiple depths simultaneously (Amir et al., 2007; Cheng et al., 2011; Göbel et al., 2007; Kerlin et al., 2010; Grewe et al., 2011). However, these techniques do not allow scanning at high resolution across more than a few hundred microns in depths. Acutely implanted microprisms have been used for wide-field epifluorescence imaging of bulk calcium activity of the apical dendrites of layer 5 neurons (Murayama et al., 2007), following acute insertion into superficial cortical layers. However, the use of epifluorescence imaging precluded visualization of individual neurons. Although our current microprism approach provides a means for chronic monitoring of activity in individual neurons and processes using two-photon calcium imaging, it is also compatible with chronic epifluorescence imaging simultaneously across a large, 1 mm × 1 mm field of view (Figure 1B), providing a useful means for rapid mapping of bulk calcium or autofluorescence signals across all cortical layers.

## Technical Outlook and Applications

Advances in a variety of optical techniques for neurophysiology hold promise for rapid advances in systems neuroscience research. The chronic microprism technique presented here can expand the capabilities of two-photon imaging by allowing simultaneous access to multiple genetically, chemically and anatomically defined neuronal populations throughout the depth of cortex. The large field-of-view available using microprisms enables high-throughput functional imaging of hundreds of neurons within local circuits of mammalian cortex. Placement of the prism face at the cortical surface of extremely medial or lateral cortical regions (data not shown) will also likely prove useful for noninvasive imaging of superficial cortical activity in hard-to-reach brain regions.

Optogenetic methods for one-photon and two-photon (Fenno et al., 2011; Prakash et al., 2012) excitation or suppression of individual neurons or local neural populations are also improving rapidly. Such methods should benefit greatly from the technique presented here, which should enable repeated photo-stimulation of neurons across cortical layers, in combination with concurrent monitoring of local neural activity. Ultimately, continued integration of microprism imaging with the above methods should provide a powerful yet relatively simple strategy for understanding interlaminar flow of information through cortical circuits in behaving animals.

## EXPERIMENTAL PROCEDURES

Experiments were performed in accordance with National Institutes of Health guidelines and were approved by the Institutional Animal Care and Use Committees at Yale and at Harvard Medical School. Male and female adult mice, 2–13 months old, were used in this study. Detailed experimental procedures for anatomical imaging (Figures 1D–1G, S1E, and S1F) and electrophysiology (Figures S2A–S2G) are described in the Supplemental Experimental Procedures. Procedures for calcium imaging experiments are described below.

### Microprism Assembly

Glass microprism assemblies (see Figures 1A, S1C, and S1D) were fabricated using standard 1 mm prisms (#MCPH-1.0; Tower Optical) (Figures 1B, 1C, 2, 3,

4, 5, and 6) coated with aluminum along their hypotenuse (Figure 1A). Prisms were attached to the bottom of a 5 mm diameter round coverglass (#1 thickness) (Figures 1B, 1C, 2, 3, 4, 5, and 6; see Figures S1A–S1D for details) using Norland Optical Adhesive 71 and cured using ultraviolet light. Care was taken to avoid damaging the coating prior to insertion. The coating did not demonstrate any sign of damage following insertion for up to 4 months.

### Surgical Procedures

Eight wild-type mice (C57BL/6, Charles River) were used in GCaMP3 imaging experiments in Figures 1B, 2, 3, 4, 5, and 6. Mice were given 0.03 ml of dexamethasone sodium phosphate (4 mg/ml, intramuscularly [i.m.]) ~3 hr prior to surgery in order to reduce brain edema. Mice were anesthetized using isoflurane in 100% $O_2$ (induction, 3%–5%; maintenance, 1%–2%) and placed into a stereotaxic apparatus (Kopf) above a heating pad (CWE). Ophthalmic ointment (Vetropolycin) was applied to the eyes. Injection of atropine sulfate (0.54 mg/ml, diluted 1:10 in sterile saline, intraperitoneally) minimized respiratory secretions. Using procedures identical to those described previously (Andermann et al., 2011), a two-pronged headpost and imaging well were affixed to the skull, a 5 mm diameter craniotomy was performed over mouse V1 (centered ~3 mm lateral and 1 mm anterior to lambda), and 100 nl of AAV2/1.hSynap.GCaMP3.3.SV40 (Penn Core) was injected into posterior primary visual cortex (V1) at 200, 500, and 800 μm below the pial surface. A chronic cranial window was then fixed in place (see Figures S1A and S1B for details) and the mouse was allowed to recover.

The microprism assembly was implanted 1–2 weeks later. Under anesthesia, the headpost was secured in place using custom clamps (Thorlabs, Standa) aligned precisely parallel to the surgical table. This minimized subsequent prism tilt (estimated to be <3%–5%) following stereotaxic insertion of the microprism parallel to the plane of the headpost (which is parallel to the imaging plane; Andermann et al., 2010).

After headpost disinfection with 70% ethanol, the dental cement holding the cranial window in place was carefully drilled away using a sterile carbide bit (FG 4, Microcopy Dental). Debris was flushed repeatedly with sterile saline and the cranial window was removed. The cortical surface was then flushed with sterile artificial cerebrospinal fluid (ACSF) until any bleeding stopped. The dura was punctured with a microprobe and removed with #5 forceps (FST).

A sharp-tipped, straight-edge dissecting knife (FST, #10055-12) was attached to a stereotaxic arm and positioned over a region of V1 free of large surface vessels and near the center of GCaMP3 expression. The knife blade was centered over the medial aspect of the incision target, lowered 1 mm into the brain, and slowly advanced 1 mm laterally. Once the incision was made, the blade was left in place to facilitate irrigation of the incision with sterile ACSF. Once bleeding subsided, the blade was retracted and Gelfoam (Pfizer) was placed over the incision. The dissecting knife was then replaced with a custom vacuum line for gripping the prism assembly from above using suction. The prism edge was aligned with the incision, and lowered slowly until the prism was 1.1 mm below the pial surface. We ensured that sufficient pressure was applied by the cranial window on the brain regions surrounding the prism (Andermann et al., 2010). These procedures helped prevent bleeding and dural regrowth between both the brain and the coverslip and between the brain and the microprism (see Figure S2 and legend). Once the prism and cranial window assembly was in place, the window edges were affixed to the skull using Vetbond (3M), followed by C&B Metabond (Parkell) to form a permanent seal. A 1:3 dental cement mix of black powder paint (Blick) and white dental acrylic (Dentsply) was then applied for light shielding. Buprenorphine (0.05 mg/kg, i.m.) and prophylactic antibiotics (cefazolin; 500 mg/kg, i.m.; sulfatrim, 1:32 in $H_20$) were administered and the mouse was allowed to recover.

### Two-Photon and Epifluorescence Calcium Imaging

Two-photon calcium images were acquired using one of two custom-built multiphoton microscopes described previously (Figures 1B, 3, 4, and 5, 960 nm; Andermann et al., 2011; Figures 2 and 6, 920 nm; Bonin et al., 2011) using an ultrafast Ti:Sapphire laser (80 MHz; MaiTai HP Deep See, prechirped). Steering mirrors mounted on scanning galvanometers were used for all experiments except those in Figures 2 and 6, which used a resonance scanning system (4 kHz, Electro-Optical Products; Bonin et al., 2011). Calcium imaging involved a 16× 0.8 NA water immersion objective (Figures 1B, 3, 4, 5, and 6; Nikon) or a 25× 1.1 NA water immersion objective (Figure 2; Olympus), and green fluorescence was collected through a 1″ or 2″ filter (542 ± 25 nm; Semrock) in front of a photomultiplier tube (H7422P-40MOD).

### Calcium Image Acquisition and Data Analysis

For images and movies of visually evoked GCaMP3 calcium activity in neurons or axons in awake mouse visual cortex through a prism (Figures 3, 4, and 5), data were collected at 1 Hz (256 × 512 pixels spanning 600 μm in depth × 900 μm across) using ScanImage (Pologruto et al., 2003). For high-speed imaging using a resonance scanning system (Figure 6), images were collected at ~32 Hz (256 × 240 pixels) using custom software (Bonin et al., 2011) written in MATLAB (MathWorks). In all cases, each image was coregistered offline to a common target from the same session, using custom software in MATLAB (rigid-body translations; Andermann et al., 2011; Glickfeld et al., 2013). The resonance scanning system was also used for volume imaging of layer 2/3 neurons through the cranial window (Figure 2) using procedures described previously (Glickfeld et al., 2013; briefly, 25× objective (Olympus) and a piezo z scanner (Physik), scanning 31 planes separated by 3 μm (1 volume per second). During prism imaging, laser power at the objective was <70 mW (typical: ~45 mW at 205 μm from the prism face), with the exception of axon imaging at 1 day postimplant (Figures 5D–5F: 130 mW was used due to residual blood at prism and brain surfaces).

Visual stimuli consisting of local 40° Gabor-like circular patches (sigmoidal 10%–90% falloff in 10°) containing drifting square waves of varying orientation, spatial, and temporal frequency (see Figures 3 and 4 and associated text; 5 s duration, with 5 s of mean luminance between stimuli, 8–12 repetitions, pseudorandom order) were presented on a 120 Hz LCD monitor (Samsung) that was calibrated using a spectrophotometer (Photoresearch PR-650). The total recording time per session was 3–5 hr. The evoked responses for each of the 96 stimulus types was defined for each pixel in the imaging volume as the fractional change in fluorescence (ΔF/F) between [−2 s, 0 s] and [0 s, 5 s] following onset of the stimulus, averaged across trials (Andermann et al., 2011). Because baseline GCaMP3 fluorescence is sometimes dim (Andermann et al., 2011), cell masks were extracted from the maximum intensity projection of average response images (ΔF/F) across all stimulus types, using custom semiautomated segmentation algorithms. Extraction of three-dimensional cell masks in Figure 2, and analyses of active axonal boutons in Figures 5D–5F are described in detail in Glickfeld et al. (2013). For analyses in Figure 6 of V1 activity as mice stood or ran on a linear trackball (Andermann et al., 2011) in near-complete darkness, cell masks were extracted from the projection across all endogenous fluorescence transients within the 20 min recording (projection of $(F(t) - F_{median})/F_{median}$ across the image stack).

Cellular fluorescence time courses were generated by averaging all pixels in a cell mask. Neuropil signals were removed by first selecting a neuropil ring surrounding each neuron (excluding adjacent rings; Kerlin et al., 2010), estimating the common time course of all such rings in the image (first principal component), and removing this component from each cell's time course (scaled by the fluorescence of the surrounding ring). For subsequent analyses, only cells that were significantly driven by at least one stimulus type were included (t tests with Bonferroni correction; for example, $p < 0.05/96$ in Figure 3). Estimates for orientation preference (Figure 3) were obtained by vector averaging ($1/2 \times \tan^{-1}(\Sigma R_i(\theta_i)\sin(2\theta_i)/\Sigma R_i(\theta_i)\cos(2\theta_i))$, where $\theta_i$ is the orientation of each stimulus, and $R_i$ is the average response to that stimulus; Kerlin et al., 2010). Similarly, direction preference (Figure 2) was defined as $\tan^{-1}(\Sigma R_j(\theta_j)\sin(\theta_j)/\Sigma R_j(\theta_j)\cos(\theta_j))$, where $\theta_j$ denotes the direction of each stimulus, and $R_j$ is the average response to that stimulus. Direction selectivity (Figure 2) was defined as $(R_{peak} - R_{null})/(R_{peak} + R_{null})$, where $R_{peak}$ is the peak response (across 16 directions) and $R_{null}$ is the average response at 180° from peak.

## SUPPLEMENTAL INFORMATION

Supplemental Information includes Supplemental Experimental Procedures, two figures, and five movies and can be found with this article online at http://dx.doi.org/10.1016/j.neuron.2013.07.052.

## ACKNOWLEDGMENTS

We thank Lindsey Glickfeld and Vincent Bonin for assistance with resonance scanning and data analysis, Vladimir Berezovskii for assistance with histology, Demetris Roumis and Christine Mazur for surgical contributions, Jeff Curry for behavioral training, and Sergey Yurgenson, Peter O'Brien, Aleksandr Vagodny, Anthony De Simone, and Matthias Minderer for technical contributions. We thank Chris Deister, Aaron Kerlin, and members of the Reid and Andermann labs for advice, suggestions, and discussion. This work was supported by the NSF CAREER Award DBI-0953902 (M.J.L. and N.G.), Kavli Center for Neuroscience (M.W. and D.A.M.), Swebilius award (R.N.S.S), NIH (D.A.M.), NIH R01 EY018742 and EY010115 (R.C.R.), the Ludcke Foundation and Pierce Charitable Trust (M.L.A.), and the Smith Family Foundation (M.L.A.).

Accepted: July 29, 2013
Published: October 17, 2013

## REFERENCES

Adesnik, H., and Scanziani, M. (2010). Lateral competition for cortical space by layer-specific horizontal circuits. Nature *464*, 1155–1160.

Amir, W., Carriles, R., Hoover, E.E., Planchon, T.A., Durfee, C.G., and Squier, J.A. (2007). Simultaneous imaging of multiple focal planes using a two-photon scanning microscope. Opt. Lett. *32*, 1731–1733.

Andermann, M.L., Kerlin, A.M., and Reid, R.C. (2010). Chronic cellular imaging of mouse visual cortex during operant behavior and passive viewing. Front. Cell Neurosci. *4*, 3.

Andermann, M.L., Kerlin, A.M., Roumis, D.K., Glickfeld, L.L., and Reid, R.C. (2011). Functional specialization of mouse higher visual cortical areas. Neuron *72*, 1025–1039.

Antonini, A., Fagiolini, M., and Stryker, M.P. (1999). Anatomical correlates of functional plasticity in mouse visual cortex. J. Neurosci. *19*, 4388–4406.

Barretto, R.P., Ko, T.H., Jung, J.C., Wang, T.J., Capps, G., Waters, A.C., Ziv, Y., Attardo, A., Recht, L., and Schnitzer, M.J. (2011). Time-lapse imaging of disease progression in deep brain areas using fluorescence microendoscopy. Nat. Med. *17*, 223–228.

Biran, R., Martin, D.C., and Tresco, P.A. (2005). Neuronal cell loss accompanies the brain tissue response to chronically implanted silicon microelectrode arrays. Exp. Neurol. *195*, 115–126.

Bonin, V., Histed, M.H., Yurgenson, S., and Reid, R.C. (2011). Local diversity and fine-scale organization of receptive fields in mouse visual cortex. J. Neurosci. *31*, 18506–18521.

Centonze, V.E., and White, J.G. (1998). Multiphoton excitation provides optical sections from deeper within scattering specimens than confocal imaging. Biophys. J. *75*, 2015–2024.

Cheng, A., Gonçalves, J.T., Golshani, P., Arisaka, K., and Portera-Cailliau, C. (2011). Simultaneous two-photon calcium imaging at different depths with spatiotemporal multiplexing. Nat. Methods *8*, 139–142.

Chia, T.H., and Levene, M.J. (2009a). In vivo imaging of deep cortical layers using a microprism. J. Vis. Exp. Published online August 27, 2009. http://dx.doi.org/10.3791/1509.

Chia, T.H., and Levene, M.J. (2009b). Microprisms for in vivo multilayer cortical imaging. J. Neurophysiol. *102*, 1310–1314.

Chia, T.H., and Levene, M.J. (2010). Multi-layer in vivo imaging of neocortex using a microprism. Cold Spring Harb. Protoc. Published online August 1, 2010. http://dx.doi.org/10.1101/pdb.prot5476.

Denk, W., Delaney, K.R., Gelperin, A., Kleinfeld, D., Strowbridge, B.W., Tank, D.W., and Yuste, R. (1994). Anatomical and functional imaging of neurons using 2-photon laser scanning microscopy. J. Neurosci. Methods *54*, 151–162.

Dombeck, D.A., Khabbaz, A.N., Collman, F., Adelman, T.L., and Tank, D.W. (2007). Imaging large-scale neural activity with cellular resolution in awake, mobile mice. Neuron *56*, 43–57.

Dräger, U.C. (1975). Receptive fields of single cells and topography in mouse visual cortex. J. Comp. Neurol. *160*, 269–290.

Dunn, A.K., Wallace, V.P., Coleno, M., Berns, M.W., and Tromberg, B.J. (2000). Influence of optical properties on two-photon fluorescence imaging in turbid samples. Appl. Opt. *39*, 1194–1201.

Fenno, L., Yizhar, O., and Deisseroth, K. (2011). The development and application of optogenetics. Annu. Rev. Neurosci. *34*, 389–412.

Glickfeld, L.L., Andermann, M.L., Bonin, V., and Reid, R.C. (2013). Cortico-cortical projections in mouse visual cortex are functionally target specific. Nat. Neurosci. *16*, 219–226.

Göbel, W., Kampa, B.M., and Helmchen, F. (2007). Imaging cellular network dynamics in three dimensions using fast 3D laser scanning. Nat. Methods *4*, 73–79.

Grewe, B.F., Voigt, F.F., van 't Hoff, M., and Helmchen, F. (2011). Fast two-layer two-photon imaging of neuronal cell populations using an electrically tunable lens. Biomed. Opt. Express *2*, 2035–2046.

Horton, N.G., Wang, K., Kobat, D., Clark, C.G., Wise, F.W., Schaffer, C.B., and Xu, C. (2013). In vivo three-photon microscopy of subcortical structures within an intact mouse brain. Nat. Photonics *7*, 205–209.

Jung, J.C., Mehta, A.D., Aksay, E., Stepnoski, R., and Schnitzer, M.J. (2004). In vivo mammalian brain imaging using one- and two-photon fluorescence microendoscopy. J. Neurophysiol. *92*, 3121–3133.

Keller, G.B., Bonhoeffer, T., and Hübener, M. (2012). Sensorimotor mismatch signals in primary visual cortex of the behaving mouse. Neuron *74*, 809–815.

Kerlin, A.M., Andermann, M.L., Berezovskii, V.K., and Reid, R.C. (2010). Broadly tuned response properties of diverse inhibitory neuron subtypes in mouse visual cortex. Neuron *67*, 858–871.

Levene, M.J., Dombeck, D.A., Kasischke, K.A., Molloy, R.P., and Webb, W.W. (2004). In vivo multiphoton microscopy of deep brain tissue. J. Neurophysiol. *91*, 1908–1912.

MacLean, J.N., Fenstermaker, V., Watson, B.O., and Yuste, R. (2006). A visual thalamocortical slice. Nat. Methods *3*, 129–134.

Mank, M., Santos, A.F., Direnberger, S., Mrsic-Flogel, T.D., Hofer, S.B., Stein, V., Hendel, T., Reiff, D.F., Levelt, C., Borst, A., et al. (2008). A genetically encoded calcium indicator for chronic in vivo two-photon imaging. Nat. Methods *5*, 805–811.

Mittmann, W., Wallace, D.J., Czubayko, U., Herb, J.T., Schaefer, A.T., Looger, L.L., Denk, W., and Kerr, J.N. (2011). Two-photon calcium imaging of evoked activity from L5 somatosensory neurons in vivo. Nat. Neurosci. *14*, 1089–1093.

Murayama, M., Pérez-Garci, E., Lüscher, H.R., and Larkum, M.E. (2007). Fiberoptic system for recording dendritic calcium signals in layer 5 neocortical pyramidal cells in freely moving rats. J. Neurophysiol. *98*, 1791–1805.

Niell, C.M., and Stryker, M.P. (2008). Highly selective receptive fields in mouse visual cortex. J. Neurosci. *28*, 7520–7536.

Niell, C.M., and Stryker, M.P. (2010). Modulation of visual responses by behavioral state in mouse visual cortex. Neuron *65*, 472–479.

O'Connor, D.H., Peron, S.P., Huber, D., and Svoboda, K. (2010). Neural activity in barrel cortex underlying vibrissa-based object localization in mice. Neuron *67*, 1048–1061.

Ohki, K., Chung, S., Ch'ng, Y.H., Kara, P., and Reid, R.C. (2005). Functional imaging with cellular resolution reveals precise micro-architecture in visual cortex. Nature *433*, 597–603.

Olsen, S.R., Bortone, D.S., Adesnik, H., and Scanziani, M. (2012). Gain control by layer six in cortical circuits of vision. Nature *483*, 47–52.

Paxinos, G., and Franklin, K. (2001). The Mouse Brain in Stereotaxic Coordinates, Second Edition. (Waltham: Academic Press).

Petersen, C.C., and Sakmann, B. (2001). Functionally independent columns of rat somatosensory barrel cortex revealed with voltage-sensitive dye imaging. J. Neurosci. *21*, 8435–8446.

Petreanu, L., Mao, T., Sternson, S.M., and Svoboda, K. (2009). The subcellular organization of neocortical excitatory connections. Nature *457*, 1142–1145.

Petreanu, L., Gutnisky, D.A., Huber, D., Xu, N.L., O'Connor, D.H., Tian, L., Looger, L., and Svoboda, K. (2012). Activity in motor-sensory projections reveals distributed coding in somatosensation. Nature *489*, 299–303.

Pologruto, T.A., Sabatini, B.L., and Svoboda, K. (2003). ScanImage: flexible software for operating laser scanning microscopes. Biomed. Eng. Online *2*, 13.

Prakash, R., Yizhar, O., Grewe, B., Ramakrishnan, C., Wang, N., Goshen, I., Packer, A.M., Peterka, D.S., Yuste, R., Schnitzer, M.J., and Deisseroth, K. (2012). Two-photon optogenetic toolbox for fast inhibition, excitation and bistable modulation. Nat. Methods *9*, 1171–1179.

Ros, H., Sachdev, R.N., Yu, Y., Sestan, N., and McCormick, D.A. (2009). Neocortical networks entrain neuronal circuits in cerebellar cortex. J. Neurosci. *29*, 10309–10320.

Roth, M.M., Helmchen, F., and Kampa, B.M. (2012). Distinct functional properties of primary and posteromedial visual area of mouse neocortex. J. Neurosci. *32*, 9716–9726.

Sakata, S., and Harris, K.D. (2009). Laminar structure of spontaneous and sensory-evoked population activity in auditory cortex. Neuron *64*, 404–418.

Sanchez-Vives, M.V., and McCormick, D.A. (2000). Cellular and network mechanisms of rhythmic recurrent activity in neocortex. Nat. Neurosci. *3*, 1027–1034.

Smith, S.L., and Häusser, M. (2010). Parallel processing of visual space by neighboring neurons in mouse visual cortex. Nat. Neurosci. *13*, 1144–1149.

Theer, P., Hasan, M.T., and Denk, W. (2003). Two-photon imaging to a depth of 1000 micron in living brains by use of a Ti:Al2O3 regenerative amplifier. Opt. Lett. *28*, 1022–1024.

Thomson, A.M. (2010). Neocortical layer 6, a review. Front Neuroanat *4*, 13.

Tian, L., Hires, S.A., Mao, T., Huber, D., Chiappe, M.E., Chalasani, S.H., Petreanu, L., Akerboom, J., McKinney, S.A., Schreiter, E.R., et al. (2009). Imaging neural activity in worms, flies and mice with improved GCaMP calcium indicators. Nat. Methods *6*, 875–881.

Trachtenberg, J.T., Chen, B.E., Knott, G.W., Feng, G., Sanes, J.R., Welker, E., and Svoboda, K. (2002). Long-term in vivo imaging of experience-dependent synaptic plasticity in adult cortex. Nature *420*, 788–794.

Zinter, J.P., and Levene, M.J. (2011). Maximizing fluorescence collection efficiency in multiphoton microscopy. Opt. Express *19*, 15348–15362.